Interlayer coupling in $Ni_{80}Fe_{20}$/Ru/$Ni_{80}Fe_{20}$ multilayer films: Ferromagnetic resonance experiments and theory

X. M. Liu,[1] Hoa T. Nguyen,[2] J. Ding,[1] M. G. Cottam,[2,*] and A. O. Adeyeye[1,*]

[1]*Information Storage Materials Laboratory, Department of Electrical and Computer Engineering, National University of Singapore, Singapore 117576*

[2]*Department of Physics and Astronomy, University of Western Ontario, London, Ontario, Canada, N6A 3K7*

(Received 4 March 2014; revised manuscript received 3 July 2014; published 27 August 2014)

We present a systematic study of the static and dynamic magnetization behavior of interlayer-coupled $Ni_{80}Fe_{20}$(200 Å)/Ru(t_{Ru})/$Ni_{80}Fe_{20}$(100 Å) trilayers as a function of the Ru spacer layer thickness t_{Ru}. As t_{Ru} was varied in the range from 0 to 15.8 Å, we observe a strong antiferromagnetic (AFM) exchange coupling between the two ferromagnetic (FM) layers for $t_{Ru} = 5$ Å, which becomes weak for $t_{Ru} = 10$ Å. For $t_{Ru} = 14.1$ Å, the coupled magnetic system changes from AFM to FM ordering. Using broadband ferromagnetic resonance spectroscopy, we have probed the effects of the different coupling mechanisms on both the acoustic and optic magnetic modes. We found that the biquadratic exchange coupling has a negligible effect compared to Ruderman-Kittel-Kasuya-Yosida (RKKY) exchange coupling, while the uniaxial anisotropy at the $Ni_{80}Fe_{20}$/Ru interfaces also plays an important role in determining the behaviors of the modes. A mode anticrossing phenomenon is observed when the RKKY exchange interaction term is above a critical value. A theoretical framework developed is in very good agreement with our experimental results.

DOI: 10.1103/PhysRevB.90.064428 PACS number(s): 76.50.+g, 75.40.Gb, 75.70.−i, 75.30.Et

I. INTRODUCTION

The interlayer exchange coupling (IEC) between two ferromagnetic (FM) layers separated by a nonmagnetic (NM) metallic layer has attracted tremendous interest in past decades due to the potential in a wide range of applications such as giant magnetoresistance (GMR) based read heads [1,2], magnetic recording devices, and magnetic random access memory (MRAM) [3–5]. Depending on the material (e.g., Cr, Cu, Ru) [6–8] and thickness [9,10] of the NM spacer layer, either ferromagnetic or antiferromagnetic (AFM) type of interlayer coupling can be achieved in a trilayer structure. Furthermore, the precessional dynamics which determines the high-speed response of spintronic devices can also be greatly influenced by the strength and sign of the IEC [11–15]. In this regard, an understanding of IEC in these trilayer structures is of significant importance for future spintronic applications and high-speed information processing. In this paper, we present a systematic study of the influence of Ru spacer layer thickness t_{Ru} on the interlayer coupling of $Ni_{80}Fe_{20}$/Ru(t_{Ru})/$Ni_{80}Fe_{20}$ trilayer structures. Both the static and dynamic properties of the trilayer structures are investigated as a function of t_{Ru} using a vibrating sample magnetometry (VSM) and a broadband ferromagnetic resonance (FMR) microscopy, respectively.

On the theoretical side, the pioneering work of Grünberg *et al.* [6] and Baibich *et al.* [1] on trilayer systems consisting of magnetic bilayers coupled via an antiferromagnetic or oscillatory interlayer exchange through a nonmagnetic spacer prompted the need for a deeper understanding of Ruderman-Kittel-Kasuya-Yosida (RKKY) interactions [16,17]. There were notable studies made by Cochran *et al.* [18] for Fe/Cu/Fe and Zhang *et al.* [7] for Co/Ru/Co, where the authors calculated the equilibrium orientations of the layer magnetizations (taken to be spatially uniform within each magnetic layer) as the applied field was varied, as well the dynamical susceptibility. More recently, a similar analysis was made by Gonzalez-Chavez *et al.* [11] to interpret their experimental data on $Ni_{81}Fe_{19}$/Cu/$Ni_{81}Fe_{19}$.

In this work, there are several differences required for the theory. First, we allow for the magnetization direction to be variable across the thickness of each layer. Generally, the local magnetization direction lies in the plane of the layers, but is canted (or "twisted") at an angle to the applied field direction. The variability of the twisting angle with depth into the magnetic layers can be incorporated into the theory following a similar approach to that used by Camley [19,20] in studying the spin-reorientation phase transition near direct magnetic interfaces between antiferromagnetically coupled ferromagnets. In our work, the variations of the twisting angle are small as regards the field-dependent phase behavior and other static properties, but nevertheless we find that they are important to include for a realistic description of the long-wavelength dynamical properties (e.g., for the FMR modes). Another difference compared with the previous calculations [7,11,18–20] is the incorporation of both the static and dynamical aspects of the long-range magnetic dipole-dipole interactions into the theory. This is achieved by generalizing previous microscopic (Hamiltonian-based) dipole-exchange theory for single ferromagnetic thin films [21,22] to the coupled magnetic bilayers being considered here. Also, with this theoretical method, it is convenient to include other possible effects into the Hamiltonian, such as biquadratic exchange coupling across the spacer layer, which is known to be important in some materials [17,23], and various forms of single-ion magnetic anisotropy [24,25].

The paper is organized as follows: In Sec. II, we describe our experiment details including the sample fabrication process and characterization techniques. The theoretical model used

*Corresponding authors: cottam@uwo.ca; eleaao@nus.edu.sg

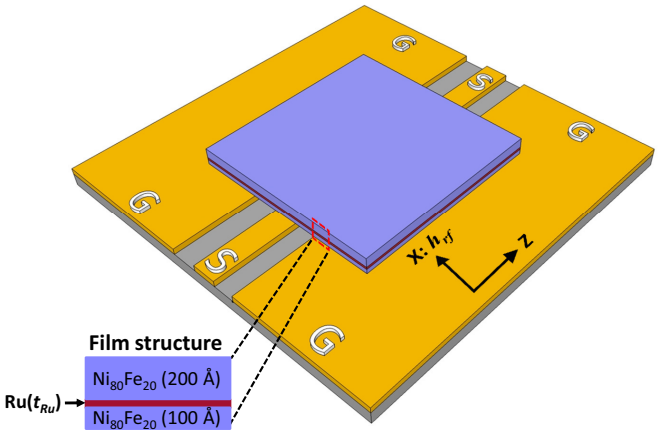

FIG. 1. (Color online) Schematics of coplanar waveguide (CPW) positioned at the bottom of $Ni_{80}Fe_{20}$(200 Å)/Ru(t_{Ru})/$Ni_{80}Fe_{20}$(100 Å) trilayer films for FMR measurements.

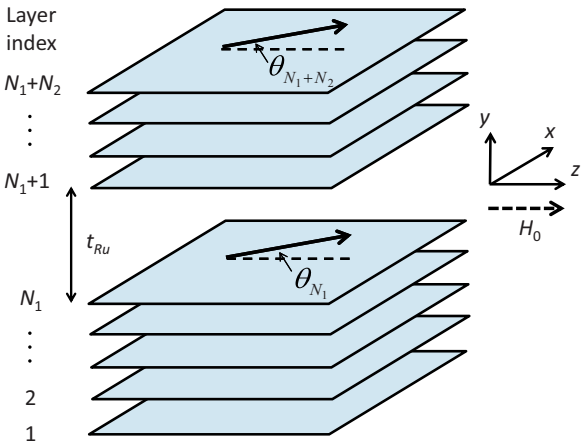

FIG. 2. (Color online) Assumed geometry for modeling the two magnetically coupled $Ni_{80}Fe_{20}$ films. The lower and upper films consist of N_1 and N_2 layers of spins, respectively, and they are separated by a Ru spacer of thickness t_{Ru}. The average spin orientation depends on the layer index n and is inclined at an angle θ_n to the z axis (applied field direction) in the xz plane, as shown.

to describe the experimental results is presented in Sec. III. The results and discussion are presented next in Sec. IV, and Sec. V contains the conclusions.

II. EXPERIMENTAL DETAILS

$Ni_{80}Fe_{20}$(200 Å)/Ru(t_{Ru})/$Ni_{80}Fe_{20}$(100 Å) trilayers with t_{Ru} varied in the range from 0 to 15.8 Å were deposited in a chamber with a base pressure better than 2×10^{-8} Torr. The $Ni_{80}Fe_{20}$ films and the Ru layer were deposited using electron-beam evaporation and dc magnetron sputtering at a rate of 0.2 and 0.05 Å/s, respectively. The working pressure of the sputtering was 3 mTorr. The $Ni_{80}Fe_{20}$/Ru/$Ni_{80}Fe_{20}$ trilayers were fabricated in subsequent deposition steps without breaking the vacuum of the chamber.

The collective magnetic switching behavior of the $Ni_{80}Fe_{20}$/Ru/$Ni_{80}Fe_{20}$ trilayer films was characterized using VSM with the field applied in the film plane. The dynamic response was measured using a vector network-analyzer (VNA) FMR setup. For FMR measurements, coplanar waveguide (CPW) was fabricated using standard optic lithography followed by deposition of Al_2O_3(50 nm)/Ti(5 nm)/Au (150 nm) and lift-off process. The $Ni_{80}Fe_{20}$/Ru/$Ni_{80}Fe_{20}$ trilayer films were then positioned on top of the CPW by flipping the samples. Shown in Fig. 1 is the schematic of the multilayer films incorporating a CPW for FMR measurements. The ports of a microwave VNA were connected to the CPW using G-S-G–type microwave coplanar probes. The FMR response was measured at room temperature by sweeping the frequency for fixed applied field H in the 1–14 GHz range. This process was repeated for a large number of H values starting from negative saturation ($H = -1400$ Oe) to positive saturation ($H = +1400$ Oe). The frame of reference used is shown in Fig. 1. The microwave magnetic field h_{rf} produced by the signal line of CPWs was applied along the x axis while the external field H was applied along two different orientations (i.e., z and x axes). We refer to the FMR setup as conventional and longitudinal configurations when H was applied along the z and x axes, respectively [12].

III. THEORY

The theory is carried out using a discrete-lattice approach to deduce the dependence of the static magnetization configuration and the dipole-exchange spin-wave frequencies on the applied magnetic field H. This is analogous to the microscopic (or Hamiltonian-based) approach used for films in Refs. [21,22], except that we now generalize to the double film with spacer geometry and we include additional effects such as the RKKY and biquadratic exchange coupling across the Ru spacer as well as more general forms of the anisotropy. The model is shown schematically in Fig. 2 where each $Ni_{80}Fe_{20}$ film is represented as a simple-cubic lattice of effective spins. For the theory it is convenient to choose coordinate x, y, and z axes related to the direction of applied field H as indicated. The lattice constant a within the plane and between planes is chosen to be smaller than the exchange length of the material, as will be explained later. We analyze a general case in which one film has N_1 layers and the other has N_2 layers, although in the present application we have a simple ratio with $2N_1 = N_2$.

The spin Hamiltonian for the $Ni_{80}Fe_{20}$/Ru/$Ni_{80}Fe_{20}$ trilayer system with an in-plane applied magnetic field may involve several possible terms, and we write the general result as $H_{\rm total} = H_{\rm ex} + H_{\rm dip} + H_Z + H_{\rm an} + H_{\rm bq}$. The first term $H_{\rm ex}$ describes the Heisenberg (bilinear) exchange

$$H_{\rm ex} = -\frac{1}{2}\sum_{in,jm} J_{in,jm}\mathbf{S}_{in}\cdot\mathbf{S}_{jm}, \qquad (1)$$

where $\mathbf{S}_{in}$ denotes the spin vector at any lattice site i in layer n (with the layers labeled as in Fig. 2) and $J_{in,jm}$ is the exchange interaction between any two sites. We take the exchange to couple only nearest neighbors (taking the value J) in either of the $Ni_{80}Fe_{20}$ films, as well as additionally to include the interlayer RKKY interaction through a term $-J_R$ coupling any site i in layer N_1 to the corresponding site in layer $N_1 + 1$. The sign convention is that $J_R > 0$ corresponds to

antiferromagnetic coupling. The next term in the Hamiltonian describes the dipole-dipole interactions that act within and between the $Ni_{80}Fe_{20}$ films:

$$H_{\rm dip} = -\frac{1}{2} g^2 \mu_B^2 \sum_{in,jm,\alpha\beta} D^{\alpha\beta}_{in,jm} S^{\alpha}_{in} S^{\beta}_{jm}, \tag{2}$$

where α and β are Cartesian coordinates defined in Fig. 2, while g and μ_B are the Landé factor and Bohr magneton, respectively. With $\mathbf{r}$ denoting the vector connecting the spin sites, the long-range dipole interaction strength is

$$D^{\alpha\beta}_{in,jm} = \left\{ |\mathbf{r}_{in,jm}|^2 \delta_{\alpha\beta} - 3 r^{\alpha}_{in,jm} r^{\beta}_{in,jm} \right\} / |\mathbf{r}_{in,jm}|^5. \tag{3}$$

The next two terms in the Hamiltonian represent the Zeeman energy due to the applied field H and the energy due to single-ion (uniaxial) anisotropy:

$$H_Z = -g\mu_B H \sum_{in} S^z_{in}, \tag{4}$$

$$H_{an} = -\sum_{in} K_n \left(S^z_{in}\right)^2 - \sum_{in} L_n \left\{ \left(S^x_{in}\right)^2 \left(S^y_{in}\right)^2 + \left(S^y_{in}\right)^2 \left(S^z_{in}\right)^2 + \left(S^z_{in}\right)^2 \left(S^x_{in}\right)^2 \right\}. \tag{5}$$

We have included the possibility of both quadratic and quartic terms in the anisotropy [24,25], where the corresponding coefficients K_n and L_n may depend in general on the layer number n in our system. For example, the anisotropy might have different properties (compared with the bulk material) at the interface layers with the Ru spacer or at the outer film surfaces. Finally, the possibility of interface biquadratic exchange (in addition to the RKKY coupling across the interface) is included through the Hamiltonian term [17,23]

$$H_{bq} = \frac{1}{2} \sum_{in,jm} J'_{in,jm} (\mathbf{S}_{in} \cdot \mathbf{S}_{jm})^2. \tag{6}$$

We assume, for simplicity, that the biquadratic interaction strength is nonzero (with value denoted by J') only between any site i in layer N_1 and the corresponding site i in layer $N_1 + 1$. In accordance with our sign convention, if $J' > 0$ the layer magnetizations at the interface would preferentially align at 90° to one another due to this term alone.

Next, we analyze the role of the above Hamiltonian terms, and in particular their competing effects with one another, as regards finding the static (equilibrium) orientations of the spins. Afterwards, we proceed with developing the spin-wave dynamics for this system.

A. Equilibrium spin configuration

In order to calculate the set of twisting angles $\{\theta_n\}$, with $n = 1,2,\ldots,N_1+N_2$, relative to the z axis for the direction of the applied field (see Fig. 2), we follow a low-temperature ($T \ll T_C$) mean-field approach. This involves replacing $\mathbf{S}_{in}$ by $(\bar{S}^x_n, 0, \bar{S}^z_n)$ for the equilibrium orientation of any spin in layer n, where $\bar{S}^x_n = S\sin\theta_n$ and $\bar{S}^z_n = S\cos\theta_n$. In this approximation, the total-energy functional, divided by the number N of magnetic sites in each layer in the xz plane, can be expressed using Eqs. (1)–(6) as

$$\begin{aligned} \bar{E} = & -\frac{1}{2} \sum_{n,m} J_{n,m}(0) \left\{ \bar{S}^x_n \bar{S}^x_m + \bar{S}^z_n \bar{S}^z_m \right\} \\ & + \frac{1}{2} g^2 \mu_B^2 \sum_{n,m} \left\{ D^{xx}_{n,m}(0) \bar{S}^x_n \bar{S}^x_m + D^{zz}_{n,m}(0) \bar{S}^z_n \bar{S}^z_m \right\} \\ & - g\mu_B H \sum_n \bar{S}^z_n - \sum_n \left\{ K_n \left(\bar{S}^z_n\right)^2 + L_n \left(\bar{S}^z_n\right)^2 \left(\bar{S}^x_n\right)^2 \right\} \\ & + J' \left\{ \bar{S}^x_{N_1} \bar{S}^x_{N_1+1} + \bar{S}^z_{N_1} \bar{S}^z_{N_1+1} \right\}^2. \end{aligned} \tag{7}$$

Here, we used the translational symmetry in the xz plane to introduce Fourier components of the exchange interaction $J_{n,m}(\mathbf{q})$, making a transformation with respect to a two-dimensional in-plane wave vector $\mathbf{q} = (q_x, q_z)$ as follows:

$$J_{in,jm} = \frac{1}{N_T} \sum_{\mathbf{q}} J_{n,m}(\mathbf{q})\, e^{i\mathbf{q}\cdot(\mathbf{r}_j - \mathbf{r}_i)}, \tag{8}$$

where $N_T = N(N_1+N_2)$ is the total number of magnetic sites in the system. There is a similar definition for the Fourier transform $D^{\alpha\beta}_{n,m}(\mathbf{q})$ of the dipole-dipole interaction strength. For the short-range exchange (coupling nearest neighbors within each $Ni_{80}Fe_{20}$ region or RKKY directly across the spacer), it is straightforward to show that it is nonzero only when $m = n$ or $m = n \pm 1$. We then have

$$J_{n,n}(\mathbf{q}) = 2J[\cos(q_x a) + \cos(q_z a)] \quad (1 \leqslant n \leqslant N_1 + N_2), \tag{9}$$

$$J_{n,n+1}(\mathbf{q}) = J_{n+1,n}(\mathbf{q}) = \begin{cases} J & (1 \leqslant n < N_1 \text{ or } N_1 + 1 \leqslant n < N_1 + N_2), \\ J_R & (n = N_1). \end{cases} \tag{10}$$

On the other hand, the dipole-dipole term $D^{\alpha\beta}_{n,m}(\mathbf{q})$ can conveniently be reexpressed as a rapidly converging series of Bessel functions [26] and then evaluated numerically [21,22].

Next, the components of the effective magnetic field $\mathbf{H}_{\rm eff}(n')$ for a spin in any layer n' can be found using Eq. (7) together with the relationships

$$H^x_{\rm eff}(n') = -\frac{1}{g\mu_B} \frac{\delta \bar{E}}{\delta \bar{S}^x_{n'}}, \quad H^z_{\rm eff}(n') = -\frac{1}{g\mu_B} \frac{\delta \bar{E}}{\delta \bar{S}^z_{n'}}. \tag{11}$$

The procedure now is to choose a starting configuration of angles $\{\theta_n\}$ to approximate the ground state. The effective field $\mathbf{H}_{\rm eff}(n')$ on any spin in a randomly selected layer n' can be found as above, and that spin can be rotated to be parallel to the local effective field, i.e., taking the new angle as $\theta_{n'} = \tan^{-1}\{H^x_{\rm eff}(n')/H^z_{\rm eff}(n')\}$. This reduces the total energy, and the process is repeated until convergence to a self-consistent configuration is achieved. Different starting configurations may be employed in order to avoid local minima and find the $T = 0$ ground state.

For the numerical application, we use realistic values for the saturation magnetization $M_s = 720$ Oe, exchange stiffness $D = 2.4 \times 10^5$ Oe nm^2, and gyromagnetic ratio $\gamma = 1.85 \times 10^{-2}$ s^{-1} Oe^{-1} of $Ni_{80}Fe_{20}$. These quantities are related to the parameters of our spin Hamiltonian by $M_s = g\mu_B S/a^3$, $D = SJa^2$, and $g\mu_B = \gamma/2\pi$. Also, we choose $a = 20$ Å for the effective lattice parameter, which is smaller than the exchange length $a_{\rm ex} = \sqrt{D/4\pi M_s} \cong 52$ Å. Hence, to model the experimental film thicknesses we take $N_1 = 5$ and $N_2 = 10$, and any spatial inhomogeneity in the film magnetism (due to varying twisting angle) can be included.

B. Spin-wave frequencies

We now consider the magnetization dynamics to calculate the spin waves and hence the FMR modes as a function of the applied field. By analogy with the procedure used for magnetic stripes in Ref. [27], the first step is to make a transformation of axes for each spin from the global (x,y,z) system to a local coordinate system (x',y',z') such that the y and y' axes are coincident and there is a rotation in the xz plane through the twisting angle θ_n for a spin in layer n. Hence, the z' axis is along the equilibrium direction of that spin. Next, the Hamiltonian is rewritten in terms of boson creation and annihilation operators using the Holstein-Primakoff representation in the *local* axes. The transformed Hamiltonian can be expanded in the form $H = H^{(0)} + H^{(1)} + H^{(2)} + \cdots$, where the general term $H^{(s)}$ involves products of s boson operators. The first term $H^{(0)}$ is just a constant (in fact, proportional to $\bar{E}$) and so does not affect the dynamical behavior, while the second term $H^{(1)}$ vanishes identically as a consequence of having defined the operators relative to the local axes. The linearized spin-wave spectrum is then described by $H^{(2)}$ and higher-order terms can be neglected. The general form is

$$H^{(2)} = \sum_{\mathbf{q}} \sum_{n,m} \left[A^{(2)}_{n,m}(\mathbf{q})\, a^{\dagger}_{\mathbf{q},n} a_{\mathbf{q},m} + B^{(2)}_{n,m}(\mathbf{q})\, a^{\dagger}_{\mathbf{q},n} a^{\dagger}_{-\mathbf{q},m} + B^{(2)*}_{n,m}(\mathbf{q})\, a_{\mathbf{q},n} a_{-\mathbf{q},m} \right], \tag{12}$$

where $a^{\dagger}_{\mathbf{q},n}$ and $a_{\mathbf{q},n}$ are boson creation and annihilation operators, respectively, at in-plane wave vector $\mathbf{q}$ and layer n. The coefficients $A^{(2)}_{n,m}(\mathbf{q})$ and $B^{(2)}_{n,m}(\mathbf{q})$ depend on the twisting angles that specify the equilibrium orientations in the layers and on the parameters of the Hamiltonian. They may be regarded as the elements of $(N_1 + N_2) \times (N_1 + N_2)$ matrices denoted by $\mathbf{A}^{(2)}(\mathbf{q})$ and $\mathbf{B}^{(2)}(\mathbf{q})$. Their explicit form for the coupled bilayer system is

$$A^{(2)}_{n,m}(\mathbf{q}) = \Delta_n \delta_{m,n} - \tfrac{1}{2} S J_{n,m}(\mathbf{q})\,[1 + \cos(\theta_n - \theta_m)] + \tfrac{1}{2} S g^2 \mu_B^2 \big[\cos\theta_n \cos\theta_m D^{xx}_{n.m}(\mathbf{q}) + D^{yy}_{n,m}(\mathbf{q}) + \sin\theta_n \sin\theta_m D^{zz}_{n,m}(\mathbf{q}) - 2\cos\theta_n \sin\theta_m D^{xz}_{n,m}(\mathbf{q})\big] + 2S^3 J'_{n,m} \cos(2\theta_n - 2\theta_m), \tag{13}$$

$$B^{(2)}_{n,m}(\mathbf{q}) = \Gamma_n \delta_{n,m} - \tfrac{1}{4} S J_{n,m}(\mathbf{q})\,[\cos(\theta_n - \theta_m) - 1] + \tfrac{1}{4} S g^2 \mu_B^2 \big[\cos\theta_n \cos\theta_m D^{xx}_{n.m}(\mathbf{q}) - D^{yy}_{n,m}(\mathbf{q}) + \sin\theta_n \sin\theta_m D^{zz}_{n,m}(\mathbf{q}) - 2\cos\theta_n \sin\theta_m D^{xz}_{n,m}(\mathbf{q}) - 2i\cos\theta_n D^{xy}_{n,m}(\mathbf{q}) + 2i\sin\theta_n D^{yz}_{n,m}(\mathbf{q})\big] + S^3 J'_{n,m}\,[\cos(2\theta_n - 2\theta_m) - \cos(\theta_n - \theta_m)], \tag{14}$$

where $J'_{n,m}$ is defined to be J' if $n = N_1 = m - 1$ or if $n = N_1 + 1 = m + 1$, and zero otherwise, for the biquadratic exchange. Also, we denote

$$\Delta_n = g\mu_B H \cos\theta_n + S K_n [3\cos^2\theta_n - 1] - 2S^3 L_n [1 - 5\sin^2\theta_n \cos^2\theta_n] + S \sum_p J_{n,p}(0) \cos(\theta_n - \theta_p) - S g^2 \mu_B^2 \sum_p \big[\sin\theta_n \sin\theta_p D^{xx}_{n,p}(0) + \cos\theta_n \cos\theta_p D^{zz}_{n.p}(0)\big] - 2S^3 \sum_p J'_{n,p} [3\cos^2(\theta_n - \theta_p) - 1], \tag{15}$$

$$\Gamma_n = -\frac{1}{2} S K_n \sin^2\theta_n + 3S^3 L_n \sin^2\theta_n \cos^2\theta_n + S^3 \sum_p J'_{n,p} \sin(\theta_n - \theta_p). \tag{16}$$

Finally, from Eq. (12), we may deduce the spectrum of discrete spin-wave frequencies. Following the matrix method detailed in Ref. [28], the positive eigenvalues of the block matrix formed by

$$\begin{pmatrix} \mathbf{A}^{(2)}(\mathbf{q}) & 2\mathbf{B}^{(2)}(\mathbf{q}) \\ -2\mathbf{B}^{(2)*}(-\mathbf{q}) & -\tilde{\mathbf{A}}^{(2)}(-\mathbf{q}) \end{pmatrix} \tag{17}$$

correspond to the $N_1 + N_2$ spin-wave frequencies, where the tilde denotes a transpose matrix. The canonical transformation of the boson operators necessary to achieve the "diagonalization" of the Hamiltonian $H^{(2)}$ can be found from the eigenvectors of the matrix in Eq. (17); this provides useful information for estimating the spectral intensities of the modes [28], if needed.

Our spin-wave analysis presented here applies very generally for two ferromagnetic films coupled across a spacer. For comparison of the theory with the FMR data, we use the expressions in Eqs. (13)–(16) for $A^{(2)}_{n,m}(\mathbf{q})$ and $B^{(2)}_{n,m}(\mathbf{q})$, taking $|\mathbf{q}| \approx 0$ for the wave vector, and we take into account just the two lowest-frequency modes deduced from the 30×30 matrix resulting from Eq. (17). It is worth mentioning that the dynamic results attained from above-discussed microscopic (or Hamiltonian-based) approach could alternatively be reproduced by micromagnetic simulations using OOMMF and

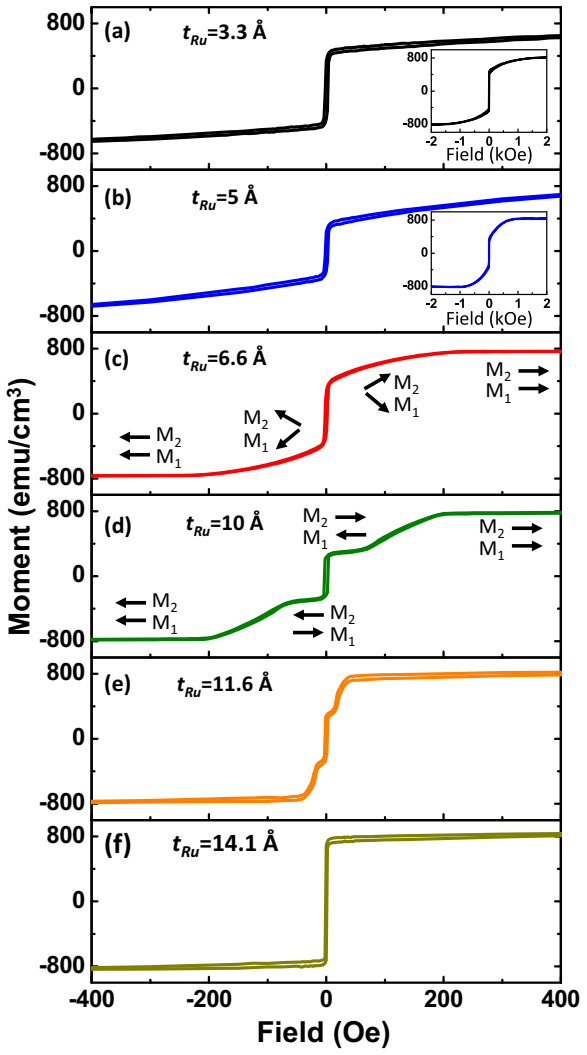

FIG. 3. (Color online) *M-H* loops of the $Ni_{80}Fe_{20}$(200 Å)/Ru(t_{Ru})/$Ni_{80}Fe_{20}$(100 Å) trilayer films as a function of t_{Ru}. (The insets show the corresponding *M-H* loops in a field range of ±2 kOe.)

COMSOL methods, as in recent comparisons of the techniques [29,30].

IV. RESULTS AND DISCUSSION

A. Static magnetic properties

Shown in Figs. 3(a)–3(f) are the *M-H* loops of the $Ni_{80}Fe_{20}$(200 Å)/Ru(t_{Ru})/$Ni_{80}Fe_{20}$(100 Å) trilayer films as a function of the Ru spacer layer thickness t_{Ru}. The *M-H* loops for the trilayers with $t_{Ru} \leqslant 6.6$ Å [Figs. 3(a)–3(c)] are similar, suggesting that the same magnetic switching process occurs in all three structures. Shown as insets in Figs. 3(a) and 3(b) are the *M-H* loops with a larger field range for $t_{Ru} = 3.3$ and 5 Å, respectively. We will take the *M-H* loop for $t_{Ru} = 6.6$ Å as an example to explain the switching process of the trilayers. Also shown as insets in Fig. 3(c) are the schematics of the magnetic orientation in the layers, where M_1 and M_2 represent the magnetizations of the 100- and 200-Å $Ni_{80}Fe_{20}$ layers, respectively.

The *M-H* loop starts with a saturated state when a high negative field is applied. Both the $Ni_{80}Fe_{20}$ layers are magnetized along the negative direction. The net magnetization decreases gradually as the value of external field (H) is reduced from negative saturation due to the formation of a spin-flop phase [12]. The appearance of a spin-flop phase is just analogous to the phase behavior in simple two-sublattice antiferromagnets with uniaxial anisotropy [31]. A similar spin-canted phase (or "flop" phase) was analyzed for a Gd/Fe bilayer system, treating the materials as ferromagnets coupled by an antiferromagnetic exchange across an interface [19], i.e., the spacer thickness is zero. The sharpness of this field-induced transition can be modified by single-ion-type anisotropy in the system. A similar approach for a Fe/Cu/Fe trilayer system was employed in Ref. [18], where both RKKY (bilinear) exchange across the spacer and single-ion anisotropy at the Fe/Cu interfaces were taken into account. The magnetization within each magnetic film was approximated as being uniform and biquadratic exchange coupling was ignored in this treatment. The authors deduced that at very low values of the applied field H the magnetizations in the magnetic films were antiparallel (antiferromagnetic state). With increasing H there is a transition first to a spin-flop phase, where the magnetization directions are roughly antiparallel to one another and transverse to H, and then at a larger field to a ferromagnetic state where the magnetizations are aligned with H. Our analysis of the static behavior given in Sec. IIIA can be modified to reach similar conclusions, e.g., if we simplify our theory by constraining all the canting angles to have a common value in one $Ni_{80}Fe_{20}$ film and a different (but common) value in the other film, ignoring the biquadratic exchange coupling.

Alternatively, a spin-flop phase can be explained by the presence of a significant biquadratic coupling in the trilayer structures, for example, as in Ref. [12]. Hence, as modeled in Sec. III, the magnetization states of the two $Ni_{80}Fe_{20}$ layers depend on the interlayer exchange coupling which may include both bilinear coupling (J_R) and biquadratic coupling (J'). This is in addition to the long-range dipolar coupling across the spacer, which is very small as regards the static magnetic properties but is important (see later) for the dynamical behavior. As discussed earlier, the interface bilinear coupling (from RKKY) favors antiparallel alignment of the magnetization while biquadratic coupling prefers a 90° alignment of the two layers. Competing effects may arise due to the single-ion anisotropy terms, depending on the strength and sign of the coefficients. In general, if J' is much smaller than J_R, the trilayer structure tends to form an antiparallel alignment of magnetization when H is sufficiently small. However, at small Ru spacer layer thickness (3.3 Å $\leqslant t_{Ru} \leqslant$ 6.6 Å), it is possible that J' may become comparable in magnitude to J_R, as attributed for the samples in Ref. [4], and the spin-flop phase would then be favored. In the spin-flop phase, the angle difference between the magnetizations of the two $Ni_{80}Fe_{20}$ layers increases as the value of H is decreased. This leads to the gradual decrease of net magnetization. A sharp magnetic switching can be observed at around zero field. This is due to the directional change of the spin-flop phase when a positive H is applied. The two $Ni_{80}Fe_{20}$ layers are then magnetized along the positive direction with a high positive field. The saturation field H_{sat} contains important information

about the AFM coupling strength. The H_{sat} of the trilayers decreases significantly from 1400 to 200 Oe as t_{Ru} is increased from 3.3 to 6.6 Å. This indicates a large decrease in AFM coupling strength.

The *M-H* loop for $t_{Ru} = 10$ Å [Fig. 3(d)] shows a plateau region (~60 Oe) after the gradual decrease of net magnetization as H is further increased. This suggests the transition of magnetization from the spin-flop phase to an antiparallel alignment of moments between the two $Ni_{80}Fe_{20}$ layers [32], which can be further verified by the magnetic moment change. The net magnetization drops to one third of the saturation magnetization due to the switching of the 100-Å $Ni_{80}Fe_{20}$ layer. The appearance of the antiparallel alignment of magnetization might indicate that the bilinear coupling dominates the interlayer exchange coupling in the trilayer structure. At the magnetic switching around zero field, the trilayer stack undergoes a 180° switching process, where the two $Ni_{80}Fe_{20}$ layers exchange the magnetization direction. This leads to a change of sign of the net magnetic moment. Further increase in the positive field results in a parallel alignment of the two $Ni_{80}Fe_{20}$ layers again. The *M-H* loop for $t_{Ru} = 11.6$ Å [Fig. 3(e)] resembles that for $t_{Ru} = 10$ Å, suggesting that the same magnetization reversal mechanism is involved. The much smaller H_{sat} (40 Oe) and plateau region (~12 Oe) indicate a much weaker AFM coupling strength in the trilayer stack. Further increasing t_{Ru} to 14.1 Å [Fig. 3(f)], we observe a clear single-step switching because the interlayer coupling has changed to ferromagnetic type.

From the theory we conclude that taking account of the variations of the twisting angle θ_n with each film can be important in some cases, depending on the RKKY coupling strength and the applied field value. Using values for the parameters as deduced from the dynamical behavior in the next subsection, we show in Table I some calculated values when $t_{Ru} = 3.3$ Å, which is the sample where the RKKY interaction is strongest. By contrast, for the sample with $t_{Ru} = 14.1$ Å where the RKKY interaction is smallest, the variation in the twisting angle is negligibly small (<1°) for the same applied field.

TABLE I. Calculated dependence of the twisting angle θ_n on the layer index n, which is defined in Fig. 2. Here, $n = \{1, 2, \ldots, 5\}$ refers to layers in the 100-Å film while $n = \{6, 7, \ldots, 15\}$ refers to the 200-Å film. These values of the angle correspond to the experimental sample with $t_{Ru} = 3.3$ Å when $H = 1200$ Oe.

Layer index n	Angle θ_n (deg.)
15	17
14	18
13	18
12	19
11	20
10	21
9	23
8	25
7	28
6	31
5	−45
4	−43
3	−41
2	−38
1	−38

In summary, it is difficult to distinguish unambiguously, on the basis of the static magnetic properties alone, between the roles played by RKKY bilinear exchange and biquadratic exchange, especially if single-ion anisotropy is present. By contrast, their roles are more distinctive as regards the magnetization dynamics, as we discuss in the following.

B. Dynamic magnetic properties

In the previous subsection, we discussed the magnetization reversal and spin flop of the $Ni_{80}Fe_{20}$/Ru/$Ni_{80}Fe_{20}$ trilayer structures as a function of the Ru spacer layer thickness. We will now turn attention to the dynamic response by focusing on three representative trilayer structures with $t_{Ru} = 5$, 10, and 14.1 Å. These three cases are deduced to correspond to strong AFM exchange coupling, weak AFM exchange coupling, and overall FM ordering of the two $Ni_{80}Fe_{20}$ layers, respectively.

1. *Strong AFM exchange coupling ($t_{Ru} = 5$ Å)*

Shown in Figs. 4(a)–4(d) are the representative FMR absorption curves taken at various fields for the $Ni_{80}Fe_{20}$/Ru/$Ni_{80}Fe_{20}$ trilayer structure with $t_{Ru} = 5$ Å. For each field value, the results with two different applied field orientations are presented, i.e., conventional FMR for H applied perpendicular to the h_{rf} direction and longitudinal FMR for H applied along the h_{rf} direction. At $H = -600$ Oe [Fig. 4(a)], only one absorption peak can be observed for conventional FMR, while two distinct absorption peaks can be clearly identified for longitudinal FMR. The peak for

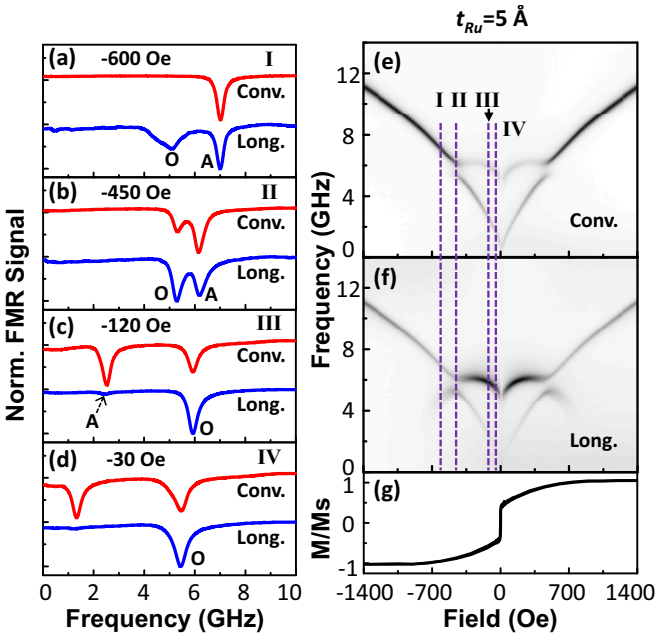

FIG. 4. (Color online) (a)–(d) FMR absorption curves at various applied fields; (e) 2D FMR spectra for conventional FMR; (f) longitudinal FMR; and (g) corresponding *M-H* loop of the $Ni_{80}Fe_{20}$/Ru(t_{Ru})/$Ni_{80}Fe_{20}$ trilayer with $t_{Ru} = 5$ Å.

conventional FMR and the higher-frequency peak for longitudinal FMR have the same resonance frequency, suggesting that this mode originates from the in-phase spin precession of the two $Ni_{80}Fe_{20}$ layers. The lower-frequency mode for longitudinal FMR is the optic mode. Two reasons may be responsible for the appearance of this optic mode. First, the formation of spin-flop phase makes the z component of the static magnetization in the trilayer structure nonzero. Second, the FMR configuration at longitudinal FMR, in which the rf field (h_{rf}) is parallel to H, is more sensitive to the signal of an optic mode [12], because the magnetization components of the $Ni_{80}Fe_{20}$ layers which are parallel to h_{rf} are added to each other in the case of 180° out-of-phase spin precession. The FMR measurement for conventional FMR is more sensitive to the in-phase spin precession (i.e., an acoustic mode) because only the magnetization components of the in-phase spins are added.

For $H = -450$ Oe, two absorption peaks can be observed for both conventional and longitudinal FMR, as shown in Fig. 4(b). There is a 0.88-GHz frequency difference between the two modes. The intensity of the lower-frequency mode for longitudinal FMR is higher than that for conventional FMR, while the higher-frequency mode is stronger for conventional FMR. This suggests that the optic mode still has a lower frequency than that of the acoustic mode. On further decreasing the field value to −120 Oe [Fig. 4(c)] and −30 Oe [Fig. 4(d)], the two modes observed in Fig. 4(b) shift to a lower resonance frequency. However, it is observed that the intensity of the lower-frequency mode becomes much stronger for conventional FMR compared to that for longitudinal FMR. It seems that the acoustic and optic modes exchange their position and amplitude when compared with the corresponding FMR curve taken at $H = -600$ Oe [Fig. 4(a), longitudinal FMR]. The frequency difference between the two modes significantly increases to 3.4 GHz for $H = -120$ Oe and 4.1 GHz for $H = -30$ Oe. This may be due to the continuous increase of magnetization angle between the two $Ni_{80}Fe_{20}$ layers in the spin-flop phase. The acoustic mode becomes extremely weak at $H = -120$ Oe and it is not observed at $H = -30$ Oe for longitudinal FMR.

We have further studied the mode evolution of this trilayer structure as a function of field. Shown in Figs. 4(e) and 4(f) are the two-dimensional (2D) FMR absorption spectra for conventional and longitudinal FMR, respectively. The darker region in grayscale represents the stronger FMR absorption. The FMR spectra are symmetric in the negative and positive field sides, consistent with the M-H loop shown in Fig. 4(g). In what follows, we focus our discussion only on the negative field side. The evolution of the mode profile is related to the different magnetization states of the two $Ni_{80}Fe_{20}$ layers. In the saturated state (-1400 Oe $< H < -800$ Oe), the magnetization states of the two $Ni_{80}Fe_{20}$ layers are aligned parallel to each other. Only one resonance mode can be observed for both conventional and longitudinal FMR due to in-phase spin precession of the two $Ni_{80}Fe_{20}$ layers. As the field value is reduced, a new weak mode appears for longitudinal FMR (around line "I"). This is the optic mode originating from the spin-flop phase of the trilayer structure. On further decreasing the field value to $H = -450$ Oe, the resonance frequency of the weak optic mode continuously increases which may possibly be associated with the increase in magnetization angle between the two $Ni_{80}Fe_{20}$ layers (e.g., by analogy with the behavior of the zero-wave-vector spin waves in the spin-flop phase of simple uniaxial antiferromagnets [33,34]). For conventional FMR, the weak optic mode is not visible in this field range between lines "I" and "II" because the FMR measurement is not sensitive to the optic mode in this setup.

A local minimum frequency can be observed in the higher-frequency mode at $H = -450$ Oe (line "II") for conventional FMR. Meanwhile, a mode with lower intensity appears with a 0.88-GHz lower frequency. An anticrossing of the two modes can be observed in the results at longitudinal FMR. At this longitudinal FMR configuration, the higher-frequency mode is much clearer than the lower-frequency mode. This suggests that the optic mode is now with a higher frequency. Furthermore, by lowering the field value (between lines "III" and "IV"), the frequency of the optic mode drops slightly while that of the acoustic mode shows a fast decrease with H, leading to the much larger frequency difference between the two modes at lower field.

2. *Weak AFM exchange coupling ($t_{Ru} = 10$ Å)*

Shown in Figs. 5(a)–5(d) are the representative FMR absorption curves taken at various applied fields for the $Ni_{80}Fe_{20}$/Ru/$Ni_{80}Fe_{20}$ trilayer structure with $t_{Ru} = 10$ Å. Only one FMR peak can be observed at both field angles for $H = -600$ Oe [Fig. 5(a)] and $H = -450$ Oe [Fig. 5(b)], suggesting the in-phase spin precession (i.e., acoustic mode) of the two $Ni_{80}Fe_{20}$ layers at saturation states. The downwards shift of resonance frequency as the field value is lowered in magnitude from −600 to −450 Oe can be explained using Kittel's

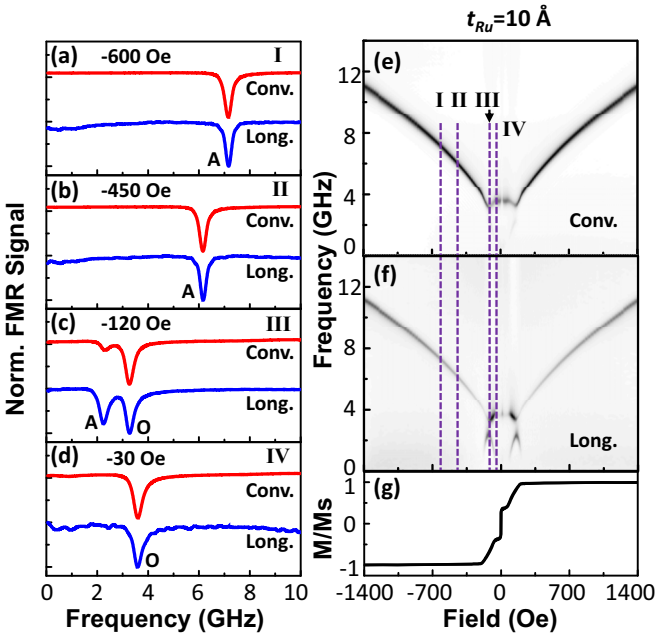

FIG. 5. (Color online) (a)–(d) FMR absorption curves at various applied fields; (e) 2D FMR spectra for conventional FMR; (f) longitudinal FMR; and (g) corresponding M-H loop of the $Ni_{80}Fe_{20}$/Ru(t_{Ru})/$Ni_{80}Fe_{20}$ trilayer with $t_{Ru} = 10$ Å.

equation [35]. Two absorption peaks can be observed at 2.2 and 3.2 GHz, respectively, when the field value is further decreased to $H = -120$ Oe. In agreement with our earlier discussions of Fig. 4(c), the two peaks correspond to the acoustic mode at lower frequency and the optic mode at higher frequency, respectively. The intensity of the optic mode is higher than that of the acoustic mode for both field angles, indicating the presence of a nonzero static magnetization component perpendicular to H at the low-field region. At even lower field $H = -30$ Oe, the lower-frequency mode disappears, leaving alone the higher-frequency mode at 3.6 GHz.

The corresponding 2D FMR spectra for conventional and longitudinal FMR are shown in Figs. 5(e) and 5(f). Again, we observed a good symmetry of the FMR spectra in the negative and positive field sides, and therefore we focus only on the negative side. Only one FMR mode can be observed when the field value is larger than $H_{sat} = -200$ Oe. As the field is swept down, a weak optic mode begins to appear for longitudinal FMR due to the formation of spin-flop phase in the trilayer structure. Again, the weak optic mode is not visible in this field range (-200 Oe $< H < -120$ Oe) for conventional FMR because the FMR measurement setup is not sensitive to the optic mode. At $H = -120$ Oe (line "III"), a mode anticrossing can be clearly observed for both conventional and longitudinal FMR. The optic and acoustic modes show an upwards and downwards jump in resonance frequency by 0.96 GHz, respectively, corresponding to the mode anticrossing. Interestingly, the resonance frequency of the optic mode increases monotonically across the whole field range of the spin-flop phase (-200 Oe $< H < -55$ Oe). Furthermore, by lowering the field value to $H = -55$ Oe, the trilayer structure switches from the spin-flop phase to an antiparallel alignment of magnetization between the two $Ni_{80}Fe_{20}$ layers. This stable antiparallel alignment of magnetization is responsible for the almost constant resonance frequency of the optic mode at the low-field range (-55 Oe $< H < 0$ Oe). This analysis is in good agreement with the *M-H* loop shown in Fig. 5(g).

3. FM ordering ($t_{Ru} = 14.1$ Å)

Shown in Figs. 6(a)–6(d) are the representative FMR results for the $Ni_{80}Fe_{20}$/Ru/$Ni_{80}Fe_{20}$ trilayer structure with $t_{Ru} = 14.1$ Å. Only one absorption peak can be observed for both conventional and longitudinal FMR at all the applied fields. This is a direct effect of the overall FM ordering between the two $Ni_{80}Fe_{20}$ trilayers, as a consequence of a much-diminished RKKY coupling (see the next subsection). As expected, the FMR mode shows a monotonic decrease of resonance frequency with decrease in the field value, which can be explained using Kittel's equation [35].

The 2D FMR spectra for conventional and longitudinal FMR are shown in Figs. 6(e) and 6(f), respectively. We observed a single FMR mode in the whole field range in line with the FMR curves shown in Figs. 6(a)–6(d), and the trilayer structure behaves like a single $Ni_{80}Fe_{20}$ layer. Compared with conventional FMR, the FMR spectrum for longitudinal configuration shows a much weaker intensity at the lower-field range (-200 Oe $< H < 0$ Oe). This is due to the fact that the FMR measurement for longitudinal FMR is not sensitive when the h_{rf} direction is parallel to the magnetization

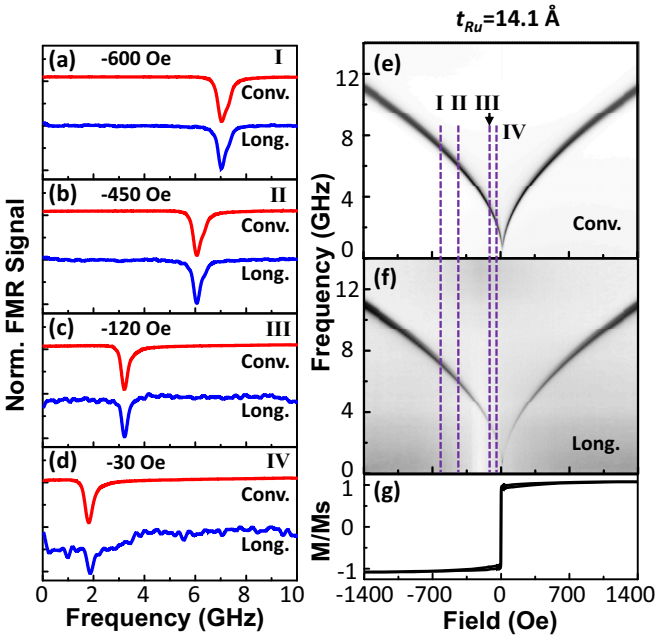

FIG. 6. (Color online) (a)–(d) FMR absorption curves at various applied fields; (e) 2D FMR spectra for conventional FMR; (f) longitudinal FMR; and (g) corresponding *M-H* loop of the $Ni_{80}Fe_{20}$/Ru(t_{Ru})/$Ni_{80}Fe_{20}$ trilayer with $t_{Ru} = 14.1$ Å.

state. The *M-H* loop shown in Fig. 6(g) agrees well with the FMR spectra shown in Figs. 6(e) and 6(f).

C. Comparison of experimental and theory results

In the previous subsection, we have shown that the conventional FMR configuration is more sensitive to the acoustic mode while the longitudinal FMR is more sensitive to the optic mode. In order to further understand the two modes, we have combined the experimental 2D FMR spectra for conventional and longitudinal FMR and analyzed them using the theory developed in Sec. III. The FMR curves are combined by adding the individual absorption curve for conventional FMR (10% intensity) and longitudinal FMR (90% intensity) at a given field. The combined FMR curves were then normalized to the maximum intensity and plotted as a function of the applied field.

The theoretical results for comparison with the experimental FMR data are found by employing the standard numerical values quoted in Sec. III for the saturation magnetization, spin-wave stiffness, and gyromagnetic ratio of $Ni_{80}Fe_{20}$. The other parameters built into the model, i.e., those referring to the interface RKKY exchange, the interface biquadratic exchange, and the single-ion anisotropy, were deduced by fitting the H dependence calculated for the lowest discrete dipole-exchange spin waves at wave vector $|\mathbf{q}| \approx 0$ to the combined FMR data as mentioned above. This was done separately for each value of the spacer thickness t_{Ru}. In practice, only the lowest two modes correspond to the frequency range of the FMR measurements (with the next calculated mode having a frequency above 30 GHz). The two modes of interest can be identified with the acoustic and optic modes that we discussed in the earlier subsections. Our calculations show that these modes do indeed

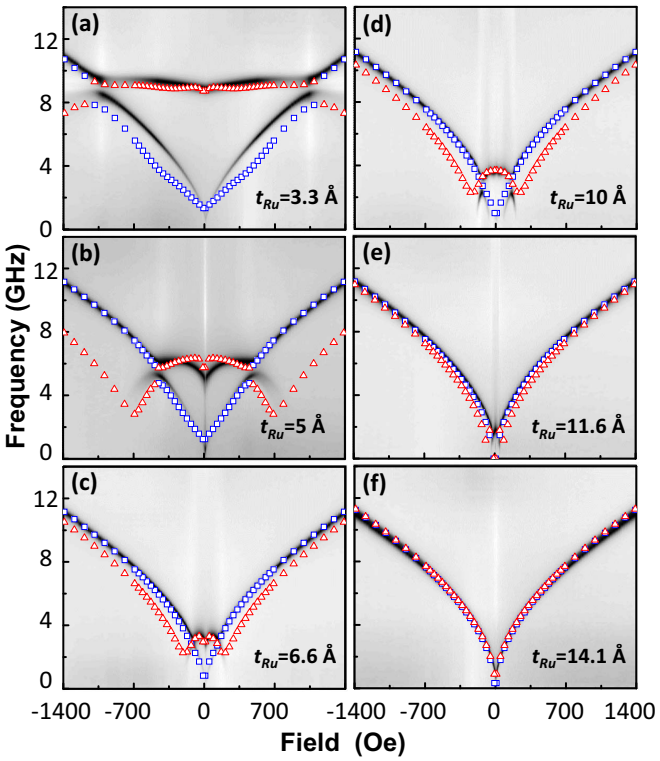

FIG. 7. (Color online) Experimental (grayscale image) and calculated (hollow symbols) 2D FMR spectra of the $Ni_{80}Fe_{20}$/Ru(t_{Ru})/$Ni_{80}Fe_{20}$ trilayer films for (a) $t_{Ru} = 3.3$ Å; (b) $t_{Ru} = 5$ Å; (c) $t_{Ru} = 6.6$ Å; (d) $t_{Ru} = 10$ Å; (e) $t_{Ru} = 11.6$ Å; and (f) $t_{Ru} = 14.1$ Å.

undergo a strong hybridization (with an anticrossing behavior) at an intermediate applied field value, as may be inferred from the three cases described in Sec. IV.B. We find that the theory leads to a good overall agreement with the FMR results over a range of values of t_{Ru}, as can be seen from Fig. 7 and discussed in more detail below. Specifically, the fitting values found for the dimensionless ratio J_R/J were -0.07, -0.03, -0.007, -0.006, -0.009, -0.002, and -0.0005 for thicknesses $t_{Ru} = 3.3$, 5, 6.6, 8.3, 10, 11.6, and 14.1 Å, respectively. The single-ion anisotropy field was found to be important only at the interface layers ($n = N_1$ and $N_1 + 1$), corresponding to $SK_n/g\mu_B$, and was equal to -0.01 T for all samples except for the 14.1-Å sample where it was taken to be zero. Also, the biquadratic exchange J' and the quartic anisotropy L_n in all layers were set to zero in these fits.

Shown in Figs. 7(a)–7(f) are the combined 2D FMR spectra (grayscale image) for the $Ni_{80}Fe_{20}$/Ru/$Ni_{80}Fe_{20}$ trilayer structures as a function of the Ru spacer layer thickness t_{Ru}. For $t_{Ru} = 3.3$ Å, a clear mode anticrossing can be observed at around $H = -1000$ Oe, as shown in Fig. 7(a). At the anticrossing point, the acoustic and optic modes show downwards and upwards shifts in resonance frequency by 0.93 GHz, respectively. The resonance frequency of the optic mode increases monotonically before the anticrossing point (-1400 Oe $< H < -1000$ Oe) due to the large angle between the average magnetizations of the two $Ni_{80}Fe_{20}$ layers. However, the variation of frequency with field is negligible afterwards (-1000 Oe $< H < 0$ Oe). The observed mode anticrossing and field-independent optic mode after the anticrossing point has been further verified by the theoretical calculation of the FMR mode, as shown in Fig. 7(a) by the hollow symbols. In this case, there is qualitative agreement between the experimental and calculated FMR results.

As t_{Ru} is increased to 5 Å [Fig. 7(b)], the mode anticrossing field shifts down to $H = -450$ Oe due to the decrease in AFM coupling strength. Interestingly, the frequency gap at the anticrossing point (0.88 GHz) also shows a slight decrease by 0.05 GHz when compared to that for $t_{Ru} = 3.3$ Å (0.93 GHz). Moreover, the resonance frequency of the optic mode for $t_{Ru} = 5$ Å shows a fast decrease in the low-field region (-200 Oe $< H < 0$ Oe). This is in direct contrast to that for $t_{Ru} = 3.3$ Å where only a slight variation of resonance frequency is observed. Here, there is good agreement between the experimental results (grayscale image) and the calculations (hollow symbols). We did not observe the optic mode above magnetic saturation in the experiment because the FMR measurement is much more sensitive to the higher-frequency mode [36].

Shown in Fig. 7(c) are the combined 2D FMR results for the trilayer structure with $t_{Ru} = 6.6$ Å. Similarly, we observed the appearance of the weak optic mode starting at the negative saturation field ($H_{sat} = -200$ Oe). The resonance frequency of this mode increases monotonically in the field range of -200 Oe $< H < -50$ Oe due to the increase in magnetization angle between the two $Ni_{80}Fe_{20}$ layers. At lower fields (-50 Oe $< H < 0$ Oe), the resonance frequency of the optic mode begins to drop. Interestingly, no mode anticrossing phenomenon was observed in this trilayer structure. The acoustic mode and the optic mode cross at $H = -110$ Oe continuously without any jump in frequency. This observation suggests that the mode anticrossing phenomenon is interlayer coupling strength dependent. It appears only when the AFM coupling strength is above a critical value. The experimental results are well reproduced by the theoretical calculation.

Further increasing the Ru spacer layer thickness to $t_{Ru} = 10$ Å [Fig. 7(d)], the mode anticrossing phenomenon appears again at $H = -120$ Oe. This might be related to the slight larger AFM coupling strength of the trilayer structure when compared to that for $t_{Ru} = 6.6$ Å. As the AFM coupling strength is lower down [$t_{Ru} = 11.6$ Å, Fig. 7(e)], the mode anticrossing phenomenon disappears. The acoustic and optic modes cross at $H = -25$ Oe without any frequency gap. For thicker Ru spacer layer [$t_{Ru} = 14.1$ Å, Fig. 7(f)], the trilayer structure has an overall FM ordering. Only one resonance mode is then observed, as expected. The above experimental observations all agree well with the calculated FMR frequencies.

Finally, we can make some useful deductions from the comparison of theory with experiment. Our fits indicate that (i) the biquadratic exchange seems to be relatively unimportant for these trilayers (and, in fact, it was ignored for the results presented in Fig. 7); (ii) a small uniaxial anisotropy acts at the $Ni_{80}Fe_{20}$/Ru interfaces (equivalent to an anisotropy field of ~100 Oe); and (iii) the RKKY exchange interaction term J_R is strongly dependent on the thickness of the Ru spacer. This last property is illustrated by Fig. 8, which shows that this antiferromagnetic exchange has its largest magnitude at the smallest values of t_{Ru}, namely, 3.3 and 5 Å. It dips in value as t_{Ru} is increased, with a small maximum at around

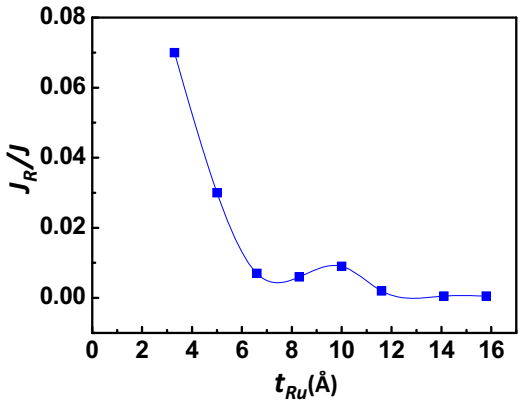

FIG. 8. (Color online) The deduced dependence of the antiferromagnetic RKKY exchange parameter J_R (relative to the ferromagnetic exchange parameter J of $Ni_{80}Fe_{20}$) on the Ru layer thickness t_{Ru}. The square symbols refer to the experimental samples and the connecting line is just a guide to the eye.

$t_{Ru} = 10$ Å before dropping to almost zero for $t_{Ru} \geqslant 11.6$ Å. It is noteworthy that a qualitatively similar behavior for a $Ni_{81}Fe_{19}$/Ru/$Ni_{81}Fe_{19}$ trilayer structure was reported by Parkin [37] for the same range of t_{Ru}. In his case, however, the dependence was deduced from the static properties (the field to achieve parallel alignment of the layer magnetizations) rather than the dynamics.

V. CONCLUSIONS

The static and dynamic magnetization behavior of interlayer-coupled $Ni_{80}Fe_{20}$(200 Å)/Ru(t_{Ru})/$Ni_{80}Fe_{20}$(100 Å) trilayer structures as a function of t_{Ru} in the range from 0 to 15.8 Å has been systematically investigated. We observed a strong antiferromagnetic (AFM) exchange coupling between the two ferromagnetic (FM) layers for $t_{Ru} = 5$ Å. It becomes weak for $t_{Ru} = 10$ Å and then the overall ordering becomes FM for $t_{Ru} = 14.1$ Å. The t_{Ru} dependence of exchange coupling also significantly affects the dynamic behaviors of the trilayer structures. A mode anticrossing of the acoustic mode and the optic mode was observed when the RKKY exchange coupling constant is above a critical value. By fitting the frequency *versus* field dependence to the FMR results using our theoretical model (which allows for the inclusion of RKKY exchange, biquadratic exchange, and magnetic dipole-dipole coupling across the Ru spacer, as well as single-ion anisotropy), the experimental FMR results were well reproduced, thus allowing us to extract various exchange coupling parameters. We found that biquadratic coupling is negligible in affecting the dynamic response although it may influence the static magnetization behavior of the trilayer structures. On the contrary, the presence of a small uniaxial anisotropy (~100 Oe) at the $Ni_{80}Fe_{20}$/Ru interfaces plays an important role in affecting the FMR modes.

ACKNOWLEDGMENTS

The support from the National Research Foundation, Prime Minister's Office, Singapore under its Competitive Research Programme (CRP Award No. NRF-CRP 10-2012-03) and the Natural Sciences and Engineering Research Council (NSERC) of Canada are gratefully acknowledged.

[1] M. N. Baibich, J. M. Broto, A. Fert, F. Nguyen Van Dau, F. Petroff, P. Etienne, G. Creuzet, A. Friederich, and J. Chazelas, Phys. Rev. Lett. **61**, 2472 (1988).
[2] C. Yu, B. Javorek, M. J. Pechan, and S. Maat, J. Appl. Phys. **103**, 063914 (2008).
[3] J.-G. Zhu, Y. Zheng, and G. A. Prinz, J. Appl. Phys. **87**, 6668 (2000).
[4] M. Belmeguenai, T. Martin, G. Woltersdorf, M. Maier, and G. Bayreuther, Phys. Rev. B **76**, 104414 (2007).
[5] D. C. Worledge, Appl. Phys. Lett. **84**, 2847 (2004).
[6] P. Grünberg, R. Schreiber, Y. Pang, M. B. Brodsky, and H. Sowers, Phys. Rev. Lett. **57**, 2442 (1986).
[7] Z. Zhang, L. Zhou, P. E. Wigen, and K. Ounadjela, Phys. Rev. B **50**, 6094 (1994).
[8] S. S. P. Parkin, N. More, and K. P. Roche, Phys. Rev. Lett. **64**, 2304 (1990).
[9] S. S. P. Parkin and D. Mauri, Phys. Rev. B **44**, 7131 (1991).
[10] P. Bruno and C. Chappert, Phys. Rev. Lett. **67**, 1602 (1991).
[11] D. E. Gonzalez-Chavez, R. Dutra, W. O. Rosa, T. L. Marcondes, A. Mello, and R. L. Sommer, Phys. Rev. B **88**, 104431 (2013).
[12] M. Belmeguenai, T. Martin, G. Woltersdorf, G. Bayreuther, V. Baltz, A. K. Suszka, and B. J. Hickey, J. Phys.: Condens. Matter **20**, 345206 (2008).
[13] H. Pham, D. Cimpoesu, A.-V. Plamadă, A. Stancu, and L. Spinu, Appl. Phys. Lett. **95**, 222513 (2009).
[14] A. Konovalenko, E. Lindgren, S. S. Cherepov, V. Korenivski, and D. C. Worledge, Phys. Rev. B **80**, 144425 (2009).
[15] S. S. Cherepov, B. C. Koop, Y. I. Dzhezherya, D. C. Worledge, and V. Korenivski, Phys. Rev. Lett. **107**, 077202 (2011).
[16] Y. Yafet, J. Appl. Phys. **61**, 4058 (1987).
[17] J. Anthony C. Bland and B. Heinrich, *Ultrathin Magnetic Structures II: Measurement Techniques and Novel Magnetic Properties* (Springer, Berlin, 1994).
[18] J. F. Cochran, J. Rudd, W. B. Muir, B. Heinrich, and Z. Celinski, Phys. Rev. B **42**, 508 (1990).
[19] R. E. Camley, Phys. Rev. B **35**, 3608 (1987).
[20] R. E. Camley and D. R. Tilley, Phys. Rev. B **37**, 3413 (1988).
[21] R. N. Costa Filho, M. G. Cottam, and G. A. Farias, Phys. Rev. B **62**, 6545 (2000).
[22] H. T. Nguyen and M. G. Cottam, J. Phys.: Condens. Matter **23**, 126004 (2011).
[23] J. C. Slonczewski, Phys. Rev. Lett. **67**, 3172 (1991).
[24] B. Heinrich and J. F. Cochran, Adv. Phys. **42**, 523 (1993).
[25] J. Anthony C. Bland and B. Heinrich, *Ultrathin Magnetic Structures I: An Introduction to the Electronic Magnetic and Structural Properties* (Springer, Berlin, 1994).
[26] H. Benson and D. L. Mills, Phys. Rev. **178**, 839 (1969).

[27] H. T. Nguyen, T. M. Nguyen, and M. G. Cottam, Phys. Rev. B **76**, 134413 (2007).
[28] T. M. Nguyen and M. G. Cottam, Phys. Rev. B **72**, 224415 (2005).
[29] K. Di, H. S. Lim, V. L. Zhang, M. H. Kuok, S. C. Ng, M. G. Cottam, and H. T. Nguyen, Phys. Rev. Lett. **111**, 149701 (2013).
[30] K. Di, H. S. Lim, V. L. Zhang, S. C. Ng, M. H. Kuok, H. T. Nguyen, and M. G. Cottam, J. Appl. Phys. **115**, 053904 (2014).
[31] N. W. Ashcroft and N. D. Mermin, *Solid State Physics* (Holt, Rinehart and Winston, Dumfries, NC, 1976).
[32] S. Wintz, T. Strache, M. Korner, M. Fritzsche, D. Marko, I. Monch, R. Mattheis, J. Raabe, C. Quitmann, J. McCord, A. Erbe, and J. Fassbender, Appl. Phys. Lett. **98**, 232511 (2011).
[33] F. Keffer, *Handbuch der Physik,* Vol. 18 (Springer, New York, 1966).
[34] M. G. Cottam and D. J. Lockwood, *Light Scattering in Magnetic Solids* (Wiley, New York, 1986).
[35] C. Kittel, Phys. Rev. **73**, 155 (1948).
[36] J. Ding, M. Kostylev, and A. O. Adeyeye, Phys. Rev. B **84**, 054425 (2011).
[37] S. S. P. Parkin, in *Ultrathin Magnetic Structures II: Measurement Techniques and Novel Magnetic Properties* edited by J. A. C. Bland and B. Heinrich (Springer, Berlin, 1994).